



1 A Portable Nitrogen Dioxide Instrument Using Cavity-Enhanced Absorption 2 Spectroscopy

3 Steven A. Bailey¹, Reem A. Hannun², Andrew K. Swanson^{1,3}, Thomas F. Hanisco¹

4

5 1. Atmospheric Chemistry and Dynamics Lab, NASA Goddard Spaceflight Center,
6 Greenbelt, MD, USA

7 2. Atmospheric Science Branch, NASA Ames Research Center, Moffett Field, CA

8 3. SciGlob Instruments and Services, LLC, Columbia, MD, USA

9

10 **Correspondence:** Steven A. Bailey (steven.a.bailey@nasa.gov)

11 Abstract

12 The Portable (2.7 kg) Cavity-enhanced Absorption of Nitrogen Dioxide (PCAND) instrument for
13 measuring *in situ* nitrogen dioxide (NO₂) was developed using incoherent, broadband cavity-
14 enhanced absorption spectroscopy (IBBCEAS). An LED light source centered at 408 nm was
15 coupled to a cavity 15 cm in length, achieving an effective optical pathlength of ~520 m. Our
16 precision was measured as 94 pptv (1 s). To date, we have flown this instrument on 3 balloon and
17 1 UAV test flights. This instrument records data to an SD card and outputs data (via an RS232
18 port) to external devices including a commercial radiosonde (iMet) for real-time data downlink.

19 1 Introduction

20 Nitrogen dioxide (NO₂) is a major contributor to air pollution in the Earth's troposphere. Its main
21 source is a byproduct of combustion from the burning of fossil fuels (Spinei, E. *et al.* 2014). NO₂
22 has been monitored from satellite instruments (like OMI, TROPOMI, and GEMS) for a decade
23 (Miyazaki, K. *et al.* 2017, Duncan, B. *et al.* 2015, Martin, R.V. *et al.* 2003, Cooper, M.J. *et al.* 2020),
24 providing a global understanding of emissions and air quality. However, satellite retrievals of the
25 total column NO₂ rely on estimates of the vertical distribution of NO₂ based on models or
26 climatology (Cersosimo, A. *et al.*, 2020). These *a priori* estimates are a major source of uncertainty



27 in making retrievals of NO₂ columns from satellite measurements (Cooper, M.J. *et al.* 2020, Dang,
28 R. *et al.* 2023).

29

30 Direct measurement of the vertical profile can verify and improve these *a priori* estimates.
31 Aircraft instruments cannot typically make a continuous vertical profile of the atmospheric
32 column. Therefore, an instrument small enough to fly on a balloon (or drone) is needed.
33 Techniques for measuring in situ NO₂ include Laser Induced Fluorescence (LIF)(Thornton, J.A. *et al.*
34 *al.* 2000), various-optical, absorption methods (like IBBCEAS)(Womack, C.C. *et al.* 2022, Min K.E.
35 *et al.* 2016), and chemical techniques (like chemiluminescence)(Ryerson, T.B. *et al.* 2000).
36 Although all these techniques have their pros and cons for use, we chose to focus on optical,
37 absorption methods for several reasons. First, we have successful experience using IBBCEAS in a
38 previous, ozone (O₃) based instrument (Hannun, *et al.*, 2020). Second, stability and ease of
39 calibration are desirable, which we found to be the case with the O₃ instrument. Third, the
40 technique can be scaled to a small enough size and weight to fly (via balloon or drone) into the
41 free troposphere. An instrument using LIF to measure NO₂ would (in our experience) not be
42 suitable for our purposes. Its size and weight would be too great to work with a small weather
43 balloon, despite LIF having greater sensitivity than IBBCEAS. Previously, a small NO₂ instrument
44 was developed by the Royal Netherlands Meteorological Institute (Dutch: Koninklijk Nederlands
45 Meteorologisch Instituut, KNMI) (Sluis, *et al.*, 2010). That instrument uses chemiluminescence to
46 measure NO₂, with a reported precision of 7.7 ppbv/sec. Although chemiluminescence
47 instruments fit our size and weight criteria, they suffer from a lengthy calibration procedure
48 before every flight. Additionally, an instrument using chemiluminescence does not have the
49 desired sensitivity we require.

50

51 A description of our instrument using IBBCEAS follows. Performance metrics will show our
52 instrument meets the Federal Aviation Administrations (FAA) uncontrolled, maximum allowable
53 weight (~2.7 kg) for a balloon payload. In addition, we record sensitivity to NO₂ that exceeds the
54 KNMI sonde by more than an order of magnitude. A description of our calibration procedure is
55 detailed showing its simplicity. Finally, we demonstrate an atmospheric vertical profile



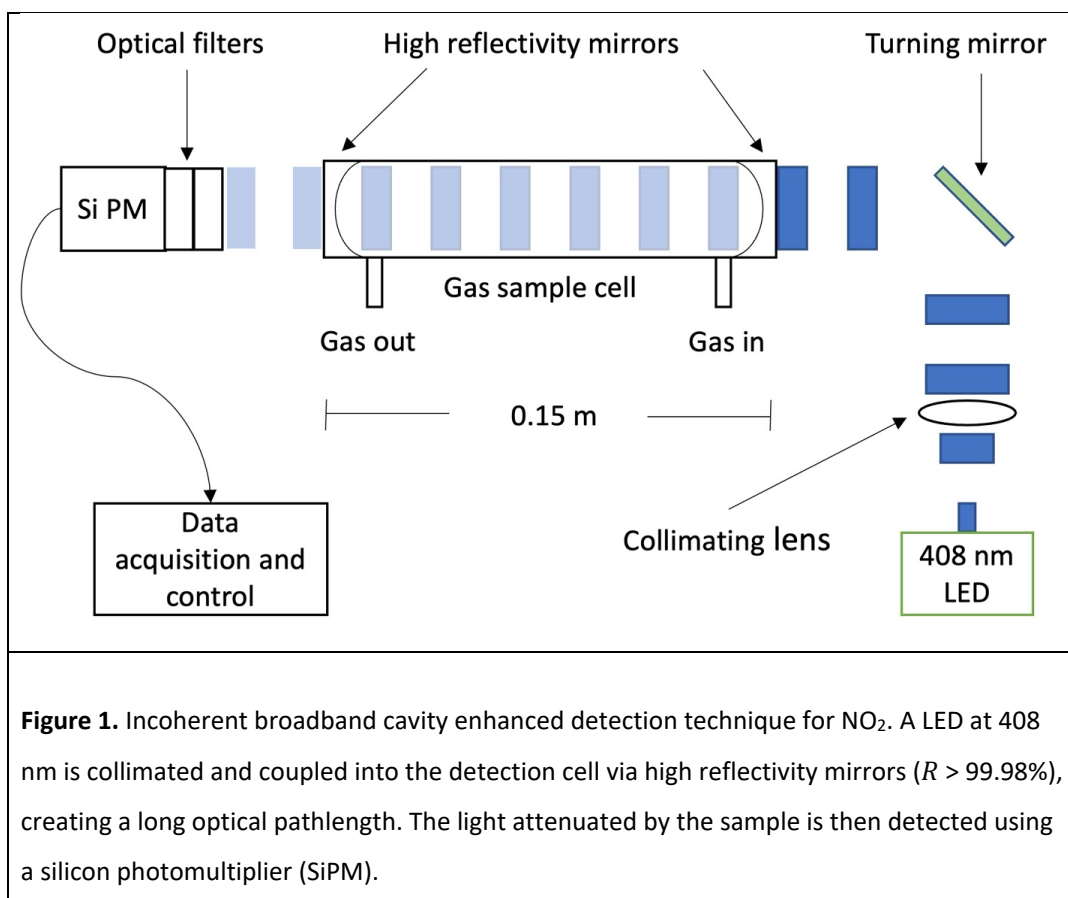
56 measurement from one of our balloon flights. We also validate our instrument via a ground-
57 based comparison with another established NO₂ instrument.

58 **2 Principle of operation**

59 IBBCEAS is an established technique for the detection of trace gases (Fiedler *et al.*, 2003; Ball *et*
60 *al.*, 2004; Washenfelder *et al.*, 2008) including NO₂ (Min *et al.*, 2016). We use an LED as our
61 incoherent, broadband light source centered at 408 nm. This is coupled to an optical cavity with
62 highly reflective mirrors on either end. IBBCEAS leverages the mirror reflectivity to turn a
63 physically short path length (15 cm) of the cavity into an effective optical pathlength of ~520 m.
64 This effective pathlength increases the probability of NO₂ absorption in the cavity, thereby
65 increasing the sensitivity (94 pptv @ 1 s) of the instrument.

66

67 Shown in Figure 1, output from an LED is collimated into the gas sample cell (cavity) where it first
68 passes through the leftmost mirror. Both mirrors have highly reflective coatings (>99.9%) on
69 curved surfaces (r=250 mm) facing towards each other. Only a small fraction of light enters the
70 cell, but the light (photons) bounces back and forth between both mirrors thousands of times on
71 average before exiting the rightmost mirror. Photons that exit are then detected by a silicon
72 photomultiplier (SiPM). A transconductance amplifier is then used to convert small amounts of
73 current from the SiPM into measurable voltage levels. A micro controller with a 12-bit analog to
74 digital convertor digitizes this voltage. The micro controller is both a data acquisition system and
75 a controller of the LED and 3-way valve. A digital lock-in scheme is used to remove background
76 light by modulating the LED at 100 Hz with a large duty cycle (70%).



77

78 Trace gas absorption (using IBBCEAS) is a measurement of light attenuation. As light is absorbed
 79 and scattered (via Rayleigh), an attenuation of light is seen at the SiPM. The Beer-Lambert
 80 absorption coefficient, α_{abs} , is directly related to the light intensity exiting the cavity
 81 (Washenfelder *et al.*, 2008; Hannun *et al.*, 2020) through the equations:

82

$$83 \quad \alpha_{abs} = \left(\frac{I_0 - I}{I}\right) \left(\frac{1 - R}{d} + \alpha_{Ray}\right) \quad (1)$$

$$84 \quad \alpha_{cav} = \left(\frac{1 - R}{d}\right) \quad (2)$$

$$85 \quad L_{eff} = \left(\frac{1}{\alpha_{cav}}\right) \quad (3)$$

86



87 Here I_0 is the intensity of light in the absence of any absorbing molecules, I is the intensity of
88 light including absorbing molecules, R is the mirror reflectivity, d is the physical distance between
89 cavity mirrors, and α_{Ray} is the extinction due to Rayleigh scatter. The term $(1 - R)/d$ is the
90 theoretical cavity loss, α_{cav} . L_{eff} represents the maximum effective pathlength. In the case of
91 mirrors with $R=0.9997$, the maximum theoretical L_{eff} for our 15 cm cell would be 450 m.

92 **3 Instrument description**

93 PCAND is housed in a small aluminum box measuring 38 cm length x 22 cm width x 7 cm height
94 with a total weight of 2.7 kg. Inside the box (Figure 2) is an optical plate where all the instrument
95 components are mounted. Power comes from an 11.1 volt Lithium Ion rechargeable battery with
96 2200 mAh (24 Wh) of storage. Table 1 summarizes the PCAND design and performance
97 characteristics.

98

99 Table 1. Summary of PCAND performance capabilities

Specification	Value
Size	38 x 22 x 7 cm
Weight	2.7 kg
Power	< 6 W
Data rate	1 Hz
Precision (1σ , 1Hz)	2.3×10^9 molec. cm^{-3}
Accuracy	6.0%
Time response	3 s

100

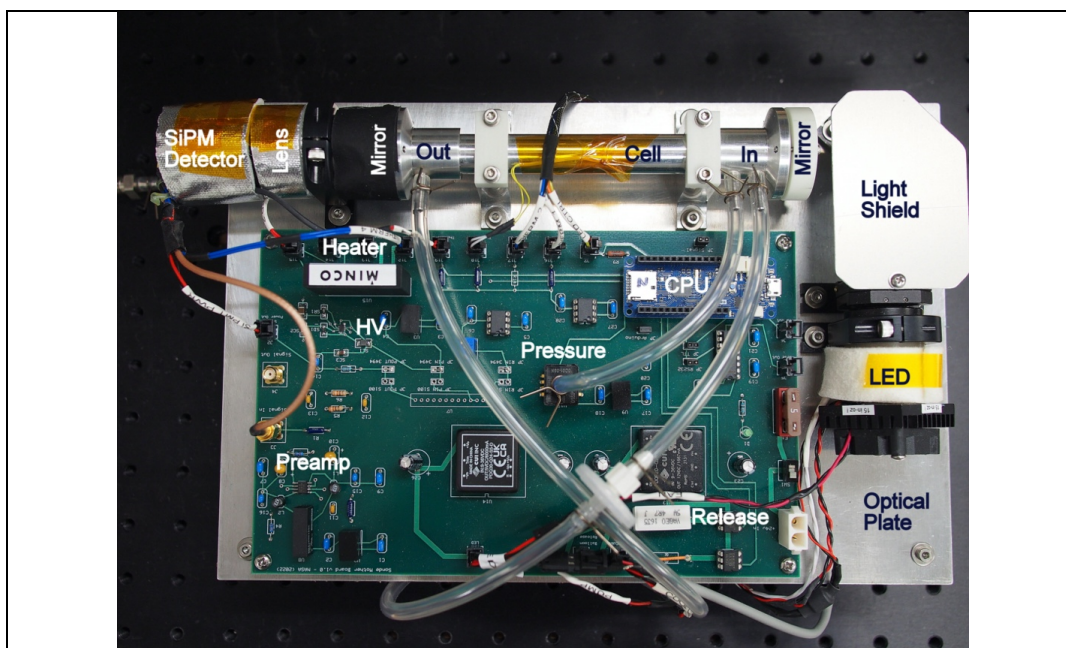


Figure 2. A top view of the NO₂ instrument. Major components include A) the optical plate, which consists of the LED assembly, light shield, turning mirror (under light shield), the optical cell, end mirrors, collimating lens, and SiPM detector; B) The electronics motherboard with detector preamp, heater controller, pressure sensor, balloon release circuit, and the data acquisition system (CPU). Not shown is the nafion tubing used to dry the air before entering the instrument.

101

102 3.1 Optical components

103 3.1.1 LED assembly

104 A UV LED ($\lambda_{\text{max}} = 408 \text{ nm}$, FWHM = 30 nm) (Thorlabs M310D1) is mounted to a custom heat sink
105 and temperature controlled to 25 °C with a thermo-electric cooler controller (Thorlabs
106 MTD415T). Constant current to the LED is supplied by a low noise controller (Thorlabs
107 MLD203CLN). The LED assembly includes a 15 mm focal length collimating lens (Thorlabs LA1074-
108 A) followed by a turning mirror (Thorlabs PF10-03-F01) to direct light into the sample cell.

109



110 3.1.2 Sample cell

111 The sample cell is manufactured from an aluminum alloy tube measuring 15 cm in length with a
112 1.4 cm inner diameter. The cell mirrors (Layertec 103654) have a reflectivity of $R > 99.9\%$ over
113 the detected spectral range (Figure 3) and a 250 mm radius of curvature. Mirrors are held to the
114 cell ends with bezel mounts on flanges with face seal o-ring glands. Although the mounts
115 themselves are non-adjustable, they are fabricated to hold the mirrors in a way that maximizes
116 their centricity to the cell ends. Furthermore, the incoherent light source negates the need for
117 rigid mirror alignment. A pressure transducer (Honeywell ASDXACX015PAAA5) measures the cell
118 pressure from a port near the cell inlet.

119

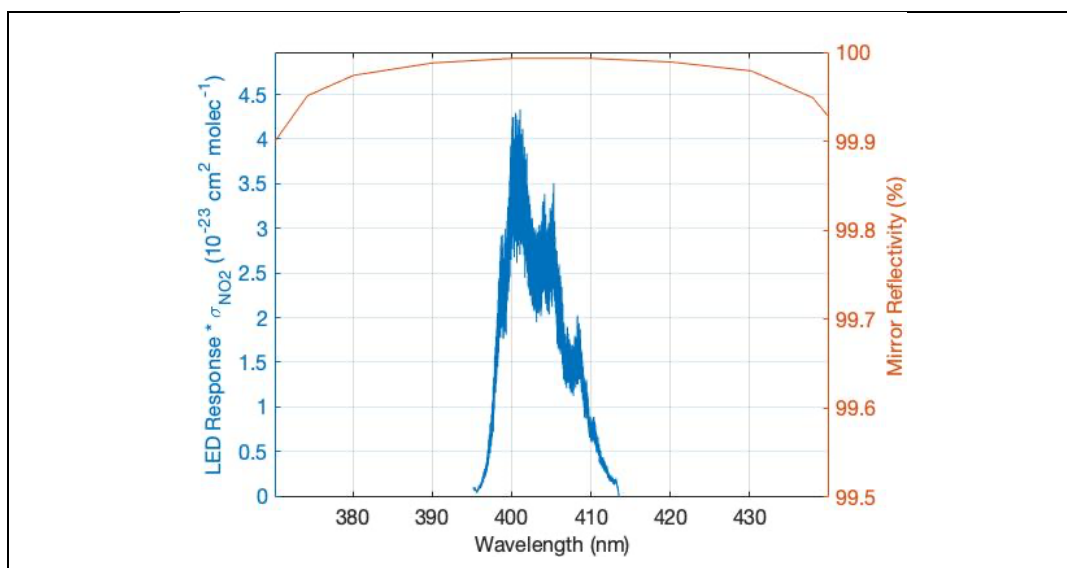


Figure 3. Normalized LED spectral response x NO₂ cross-section vs mirror reflectivity (99.98% @ 408 nm). The LED ($\lambda_{\text{max}} = 408 \text{ nm}$, FWHM = 30 nm) response was measured using a grating spectrometer with the instrument SiPM and associated detector optics. The absorption cross-section of NO₂ (for this instrument) is the integration of the above product (with a resolution of 0.0005 nm) which yields $6.0419 \times 10^{-19} \text{ cm}^2 / \text{molecule}$.

120



121 **3.1.3 SiPM assembly**

122 Following exit from the sample cell, light enters an optical bandpass filter (Semrock FF01-405/10-
123 25), then a lens (Thorlabs LA1252-A) focuses the beam onto a Silicon Photo Multiplier (SiPM -
124 Onsemi 30035) detector. The detector is biased by ~29 volts DC via a LT3494A boost converter.
125 This voltage sets the gain of this device. Signal from the SiPM is amplified through a
126 transimpedance amplifier based on a low noise, ADA4625-2 op-amp. The SiPM assembly is
127 thermally stabilized by heating it to a 35 °C setpoint using a Minco CT335 heater controller. The
128 temperature of the SiPM is monitored with a 10K thermistor mounted adjacent to the heater.
129 Temperature of the detector is held to within 0.1 °C of the setpoint using the Minco controller.

130 **3.2 Flow system**

131 The PCAND instrument uses a small, 12 volt diaphragm pump (Parker E134-11-120) to achieve a
132 1.4 standard liters per minute (SLM) flow rate. Flush time is approximately 3 seconds as evident
133 from Figure 4. A 3-way valve (ASCO 411L3212HV) is used to switch the flow between sample air
134 and scrubbed air (via an inline charcoal filter). The charcoal filter removes any NO₂ from the flow
135 and gives us our I_0 (reference) measurement every 30 seconds for 5 seconds, leaving us sample
136 air measurements 50 seconds out of every minute.

137

138

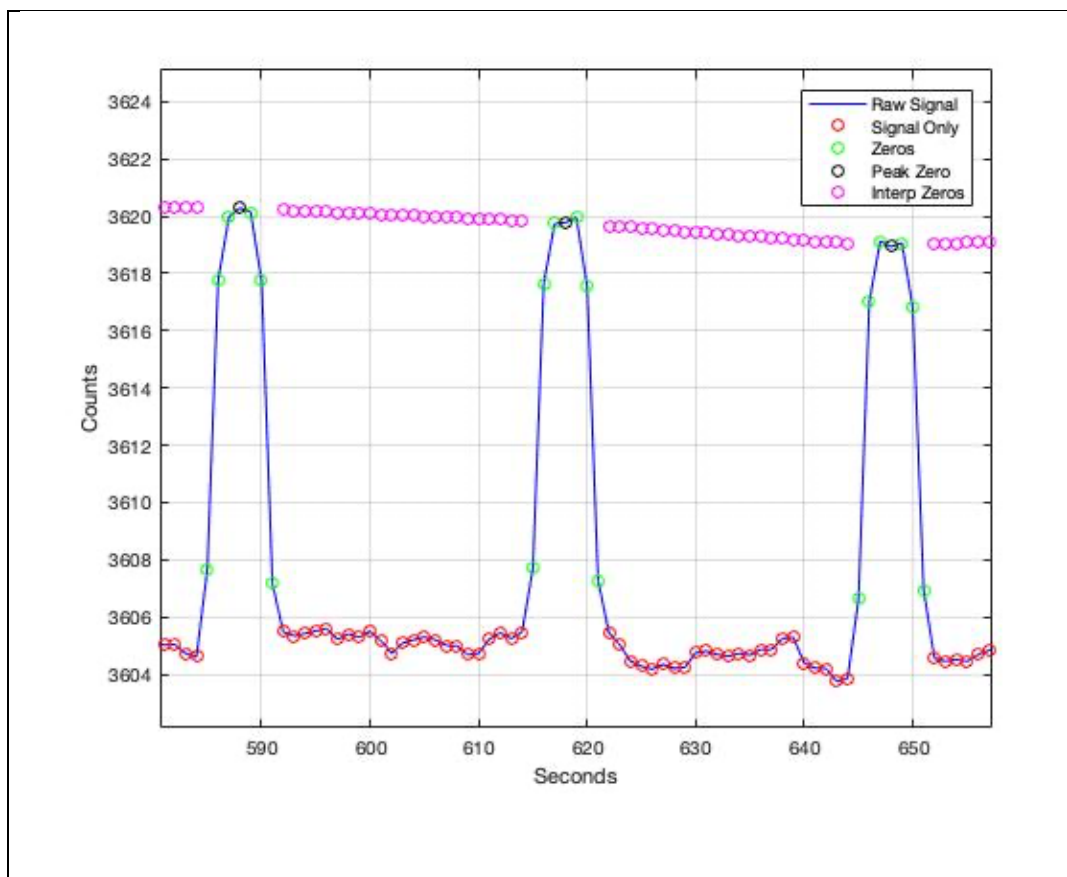


Figure 4. Cadence used to make real-time measurements of I_z (signal with no absorbers) vs I (signal with absorbers) is 7 seconds for I_z and 23 seconds for I . We found this was a good cadence allowing 3 seconds to achieve peak I_z and 3 seconds to return to I . A charcoal filter is switched into the airflow to achieve the I_z measurement.

139

140 We expect a small interference from water vapor. H_2O vapor has a cross-section of 3×10^{-17}
141 cm^2 /molecule at 405 nm (Lampel *et al.*, 2015; 2017). An atmospheric abundance of $H_2O = 1\%$
142 contributes the same absorption as 50 pptv of NO_2 . In addition, we notice stronger attenuation
143 that is not consistent with gas phase absorption like that reported in ozone instruments using
144 UV absorption (Wilson *et al.*, 2006). In principle the presence of water vapor should not affect
145 the measurement if the abundance is constant between the sample and the scrubbed air.



146 However, the scrubber material (activated charcoal) can add or remove water vapor to the
147 sampled air depending on the prior humidity. Because of this interference, water vapor is
148 removed using two 30 cm lengths of 0.3 cm diameter Nafion Dewline tubing held in an
149 enclosure with drierite. The dry air sample eliminates any contribution of water vapor in the
150 measurement.

151

152 PCAND uses fluorinated ethylene propylene (FEP) lined thermoplastic tubing for all internal
153 plumbing. A 2-micron teflon membrane filter is positioned immediately before the cell inlet to
154 keep small particles from entering the cell and potentially dirtying the mirrors.

155 **3.3 Data acquisition**

156 PCAND uses an Arduino MKR Zero microcontroller for 3-way valve control, LED modulation, and
157 data acquisition. Arduino actuation of the valve is made through a CoolCube R valve controller,
158 which reduces the holding current needed to keep the valve in its open state. LED modulation is
159 produced by the Arduino through the LED controller at a 100 Hz rate. This modulation has a 70%
160 duty cycle used to achieve a digital lock-in to remove any background light from the absorption
161 measurement. We oversample the absorption signal 42k samples / second to increase the native
162 Arduino internal 12-bit measurement to an effective (averaged over a second) ~21-bit
163 measurement. Data is recorded both to an SD card and sent to an RS-232 port. The latter is useful
164 for both instrument testing and for connecting to an external iMet radiosonde where the data is
165 merged for RF data downlink by the radiosonde.

166 **3.4 Data processing**

167 The PCAND absorbance calculation uses equation 1, but accounts for the differential cell pressure
168 between the sample flow and the zero flow, which is restricted by the scrubber. Including the
169 Rayleigh scattering for both zero air and sample air, Eq. 1 is rewritten as equation 4 (Min *et al.*
170 2016 ; Hannun *et al.*, 2020) :

171

$$172 \quad \alpha_{NO_2} = \left(\frac{I_z}{I} - 1\right) (\alpha_{cav} + \alpha_{Ray,Z}) + \Delta\alpha_{Ray} \quad (4)$$

$$173 \quad \Delta\alpha_{Ray} = \alpha_{Ray,Z} - \alpha_{Ray,S} \quad (5)$$



$$174 \quad \alpha_{Ray} = N_{air} \sigma_{Ray} \quad (6)$$

$$175 \quad \alpha_{NO_2} = N_{NO_2} \sigma_{NO_2} \quad (7)$$

$$176 \quad \alpha_{Ray,S} = \left(\frac{I_Z}{I} - 1 \right) \alpha_{cav} \quad (8)$$

177

178 Zero air is NO₂ scrubbed air where I_Z substitutes for I_0 (from equation 1). Rayleigh cavity
179 extinction is broken into 2 parts ($\alpha_{Ray,Z}$ and $\alpha_{Ray,S}$) describing zero air and sample air cavity
180 extinction respectively. In both cases, the Rayleigh scattering cross-section (σ_{Ray}), weighted by
181 the SiPMT response curve (Figure 3), is used (Bucholtz, 1995). The NO₂ number density
182 (concentration) is found by knowing the absorption cross-section of NO₂ (σ_{NO_2}) (Vandalae, 1998).

183 4 Performance

184 4.1 Sensitivity and calibration

185 The PCAND effective pathlength of the optical cavity determines the instruments sensitivity to
186 NO₂. Highly reflective mirrors on either end of the cavity are statically mounted, so no adjustment
187 of their position is required. In practice, the alignment is stable over months of operation. After
188 the initial alignment, calibration is needed to determine the effective pathlength given the mirror
189 positions. We can use equation 4 with known quantities of NO₂ to determine the effective
190 pathlength (Figure 5a). We can also use Rayleigh scattering alone to solve for effective pathlength
191 (Figure 5b). This requires varying the pressure of zero air (in the absence of NO₂) to generate a
192 data set of absorption attenuation (I) vs number density of zero air. It also requires we solve for
193 equation 8 after it has been reduced from equation 4. To do this, we must assume $\alpha_{Ray,Z}$ is taken
194 at vacuum, so $\alpha_{Ray,Z}$ goes to zero leaving only $\alpha_{Ray,S}$. We must calculate (I_Z) at vacuum using
195 our data set. This leaves us with equation 8 to solve for effective pathlength (equation 3). Using
196 known quantities of NO₂ and equation 4 yields a pathlength of 519 ± 2 m. Using the Rayleigh
197 scattering method and equation 8 yields a pathlength of 524 ± 1 m. The two methods of
198 calibration are within < 1% of each other and both yield pathlengths that agree to within 2σ
199 uncertainty for each fit. Therefore, we choose to use the Rayleigh scattering method in future
200 calibrations (when needed) of PCAND. Note that due to the small Rayleigh cross-section of air at



201 408 nm, $\sigma = 1.5 \times 10^{-26} \text{ cm}^2/\text{molecule}$ (Bucholz, 1995) the calibration using air is susceptible
202 to leaks and contamination. Adequate care must be taken to ensure that the system is free of
203 leaks and that the air is pure.

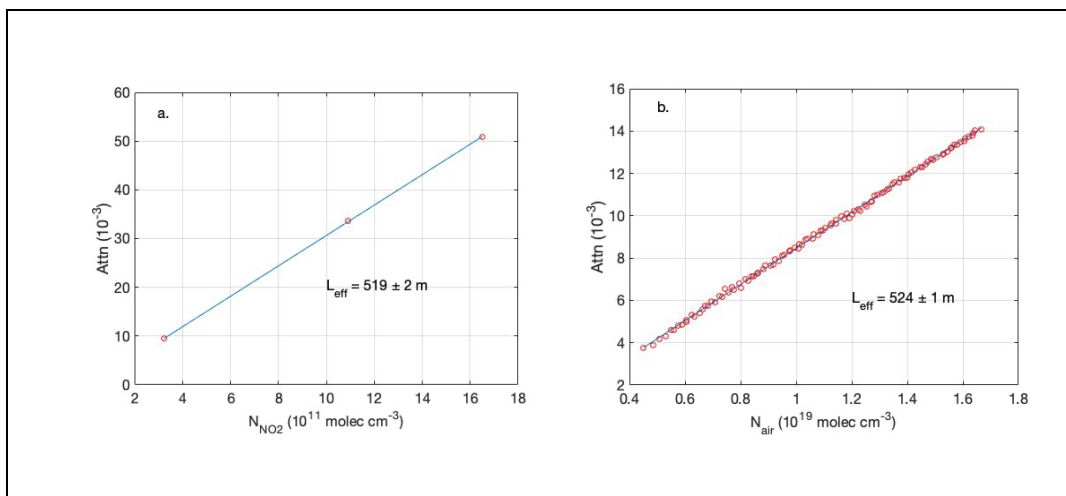


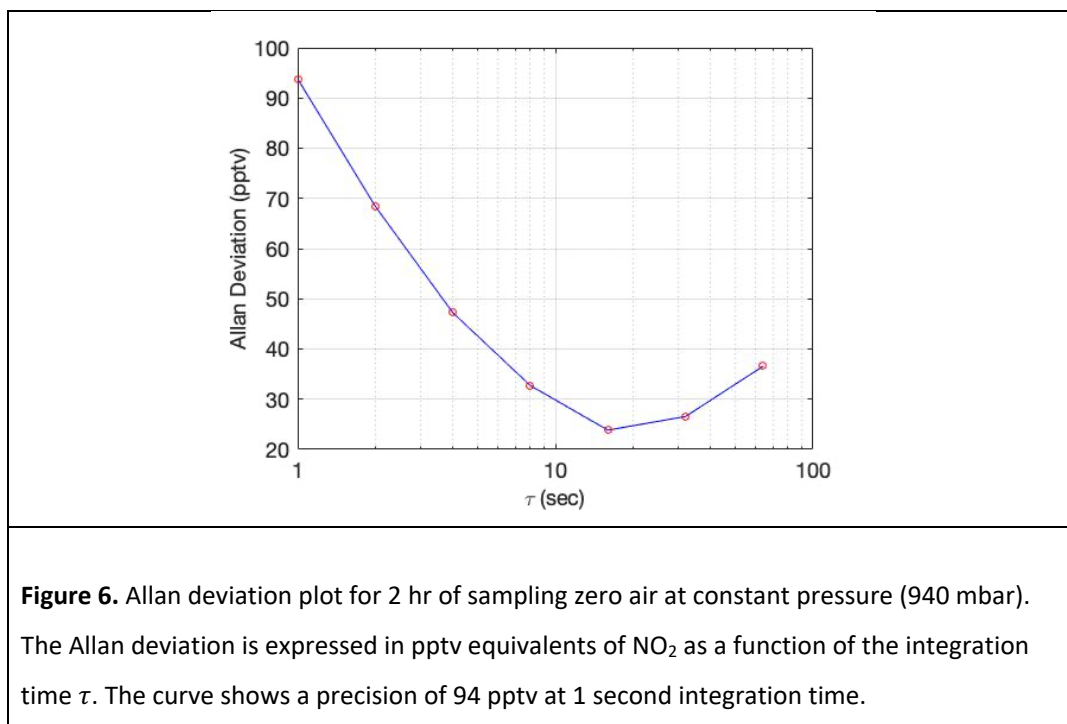
Figure 5. NO₂ Sonde calibration: a) The effective pathlength (L_{eff}) as determined by attenuation (Attn) due to known additions of NO₂ from a reference tank of NO₂ mixed with zero air. The slope yields the effective pathlength as determined from Equation 1 in the text using the known NO₂ absorption cross section; b) Attenuation due to Rayleigh scatter over a range of cell pressures. The slope of attenuation as a function of number density gives the pathlength using the known Rayleigh scattering cross-section for zero air. The pathlength from each calibration agreed to within 2σ uncertainty for each fit.

204

205 4.2 Precision and accuracy

206 The PCAND precision was determined by flowing zero air (under constant pressure of 920 mbar)
207 into the cavity for 2 hours while accumulating 1Hz data. Figure 6 is an Allan deviation plot showing
208 a 1 Hz precision of 94 pptv and a 10 s precision of 30 pptv. The 1 Hz precision translates to $2.3 \times$
209 $10^9 \text{ molecules cm}^{-3}$ of NO₂ at 1 atmosphere.

210



211

212 The accuracy of PCAND measurements depends on NO_2 and Rayleigh cross section uncertainties,
213 pressure sensor uncertainty, thermistor uncertainty, and cavity extinction uncertainty. The NO_2
214 absorption cross-section uncertainty is reported to be 3% (Spinei, 2014; Vandalae 1998). We use
215 3% for the Rayleigh scattering cross-section uncertainty (Bucholtz, 1995). From data sheets, we
216 conclude temperature and pressure measurements to have uncertainties of 0.5% and 2%
217 respectively. We also measured cavity extinction slope uncertainty at 1%. Together, the total
218 uncertainty when propagated through equation 4 comes to 6 % when applied to the final NO_2
219 number density.

220 4.3 Response time

221 Response time is a direct function of gas flush time in our cell given our small vacuum pump. A
222 flow rate of 1.4 SLM is achieved with our pump resulting in a response time of approximately 3
223 seconds (Figure 4). Given our cadence of 5 second zero followed by 25 second sample, we can
224 see (by eye) it takes ~ 3 seconds for the signal to stabilize with zero air. A larger pump could
225 shorten this response time at the expense of more mass and power needed.



226 4.4 Photolysis Effects

227 The photolysis quantum yield is 0.22 at 408 nm (*Troe, 2000*), so we expect some fraction of the
228 NO₂ in the cell to photolyze, NO₂ + hv → NO + O. In static cells the photolysis of NO₂ has been
229 shown to be a concern (*Platt et al., 2019*) In the case of our detection, it is unlikely that a
230 significant fraction of NO₂ will be photolyzed because the sample flows through the cell quickly
231 with a flush time of approximately 1 s and the number of photons available for photolysis is
232 small.

233 We can estimate the number of photons in the cell from the detector signal. The SiPM has a
234 radiant sensitivity of 4 × 10⁵ A/W and a photon detection efficiency of 50%. Based on our
235 detection signal of 2 × 10⁻⁵ A, we estimate the optical power is roughly 10⁻¹⁰ W and calculate a
236 photon flux of 2 × 10⁹ photons/s. A typical absorbance with 1 ppb NO₂ in the cell is 10⁻³, thus
237 we expect that roughly 2 × 10⁶ photons/s are absorbed by the 1 ppb NO₂ in the cell. At 900 hPa
238 the number density of 1 ppb NO₂ is roughly 2.2 × 10¹⁰ molecules/cm³. The absorption of 2 × 10⁶
239 photons would result in the photolysis of 4.4 × 10⁵ NO₂ molecules, or 2 × 10⁻⁵ of the available
240 NO₂ molecules. While this number is quite low for our conditions, it is worth noting that with
241 slower flows and higher photon fluxes the photolysis could be significant and secondary
242 chemistry could be a concern.

243 5 Field demonstration

244 PCAND was launched on 3 low altitude (~7 km) balloon flights for demonstration purposes during
245 the summer of 2022. PCAND was physically linked (via RS232 cable) to a commercial weather
246 sonde for real-time data downlink (via the weather sonde). Results from the second flight (Figure
247 7) launched on 18 August 2022 show a vertical profile of NO₂ indicative of that time of year with
248 high concentrations of NO₂ near the ground. This flight occurred at 8 am local time when the
249 boundary layer was still close to the ground. The temperature deviation in the instrument box
250 during flight to 7km was less than 1 °C.

251

252

253

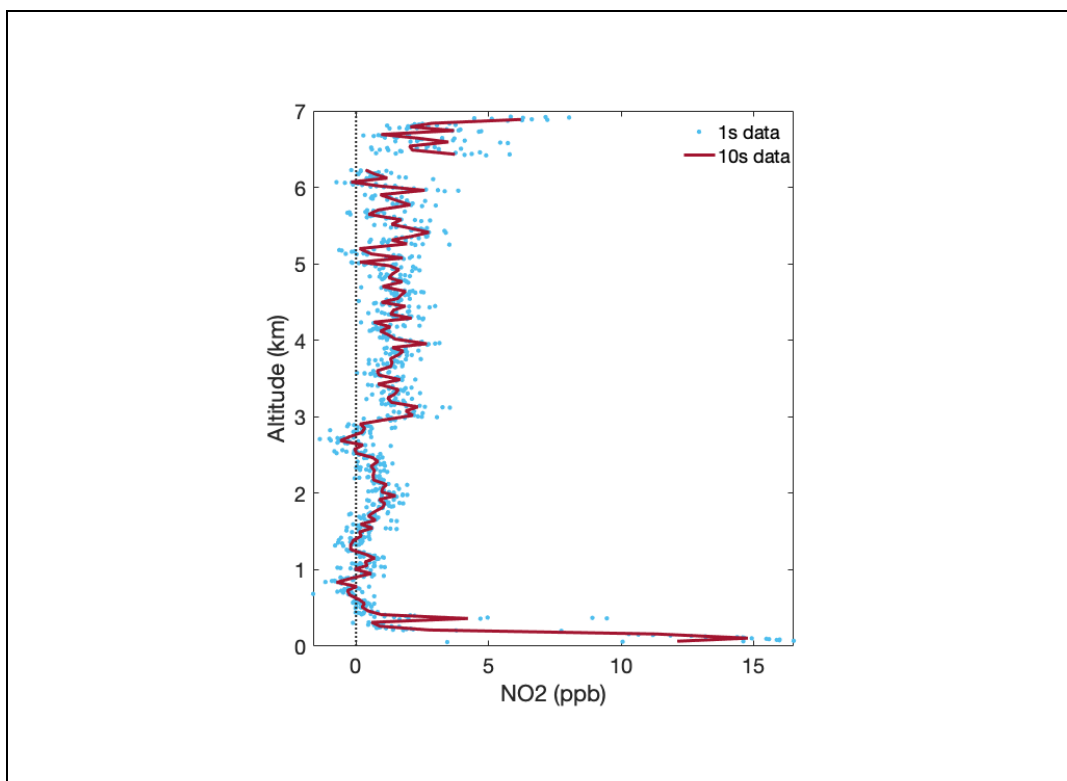


Figure 7. NO₂ Sonde flight data from 18 August 2022 balloon launch. Programmed cut-down of balloon at 7 km to achieve payload recovery. Significant concentrations of NO₂ appear near the surface and again at cut-down (~7 km) altitude.

254

255

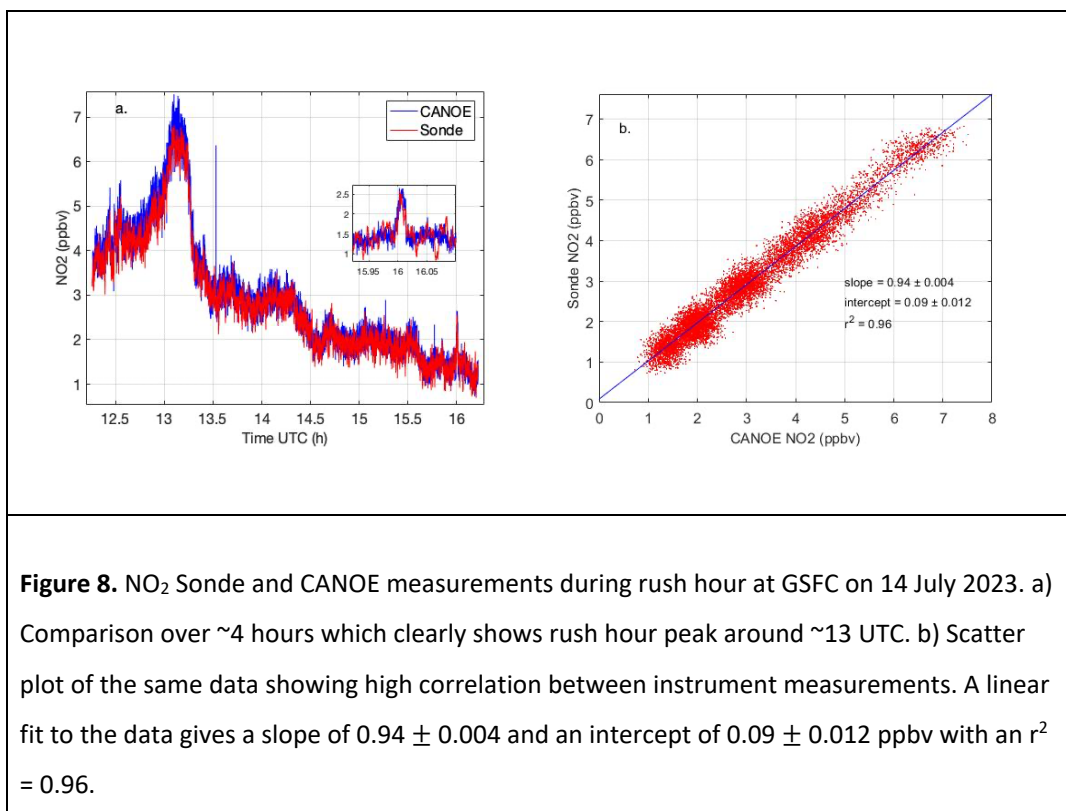
256 **5.1 Validation with CANOE**

257

258 PCAND was validated with another NO₂ instrument called CANOE (Compact Airborne Nitrogen
259 diOxide Experiment). CANOE was based on the design of a similar instrument called CAFE (St.
260 Clair *et al.*, 2019) (Compact Airborne Formaldehyde Experiment). The only difference between
261 CANOE and CAFE are the laser wavelengths (532 nm for CAFE vs 355 nm for CANOE) and PMT
262 detectors used. CANOE is an LIF instrument which has been deployed on several airborne
263 campaigns including Dynamics and Chemistry of the Summer Stratosphere (DCOTSS) and Fire



264 Influence on Regional to Global Environments and Air Quality (FIREX-AQ). CANOE has been
265 calibrated to known cylinders of NO₂ concentration. Figure 8 shows a ~4-hour data set where
266 PCAND and CANOE shared the same inlet port sampling the air during a morning in the DC greater
267 metropolitan area. Clearly, a rush hour peak of NO₂ is seen trailing off by noon. Figure 8a shows
268 good agreement between the measurements with a slope of 0.94 ± 0.004 and an intercept of
269 0.09 ± 0.012 ppbv NO₂ ($r^2 = 0.96$).



270 6 Summary and conclusions

271 PCAND provides very high sensitivity to NO₂ for such a small package using broadband cavity-
272 enhanced UV absorption at 408 nm. PCAND has a precision of ~ 94 pptv s⁻¹ with an accuracy of
273 6.0%. Although PCAND was designed for portable, battery powered operation (as needed for a
274 sonde or drone flight), it could easily be used in either ground or lab-based measurements. It was
275 successfully tested on 3 balloon flights producing NO₂ vertical profiles for each. A comparison



276 with another (calibrated) NO₂ instrument (CANOE) showed strong agreement over a ~4-hour
277 period.

278 *Author contributions.* SAB performed the investigation, controller software, electronics design,
279 testing, and wrote the paper. RAH wrote the signal processing code and determined the best
280 wavelength to use for NO₂ absorption. AKS did all the mechanical design including optical plate,
281 fixtures, and cell. TFH determined the correct mirrors to use, consulted with AKS on the optical
282 layout, and made the science case for receiving funding for this work.

283

284 *Competing interest.* At least one of the (co-)authors is a member of the editorial board of
285 Atmospheric Measurement Techniques.

286

287 *Acknowledgements.* The balloon flights were made at the Howard University Beltsville Campus
288 with the help of Adrian Flores. The drone flight was made at Virginia Commonwealth University
289 Rice Rivers Center with the help of Gregory Garman and Ron Lopez. We would additionally like
290 to thank Ryan Stauffer for his expertise in balloon flight needed to launch and recover our
291 instrument.

292

293 *Financial support.* This research has been supported by the NASA Internal Research and
294 Development (IRAD) program at Goddard Space Flight Center (GSFC).

295 **References**

296 Ball, S. M., Langridge, J. M., and Jones, R. L.: Broadband cavity enhanced absorption spectroscopy
297 using light emitting diodes, Chem. Phys. Lett., 398, 68–74,
298 <https://doi.org/10.1016/j.cplett.2004.08.144>, 2004.

299

300 Bucholtz, A.: Rayleigh-scattering calculations for the terrestrial atmosphere, Appl. Optics, 34,
301 2765–2773, <https://doi.org/10.1364/AO.34.002765>, 1995.

302

303 Cersosimo, A., Serio, C., and Masiello, G.: TROPOMI NO₂ Tropospheric Column Data: Regridding
304 to 1 km Grid-Resolution and Assessment of their Consistency with In Situ Surface Observations,
305 Remote Sens., 12, 2212, <https://doi.org/10.3390/rs12142212>, 2020.



- 306
307 Cooper, M. J., Martin, R. V., Henze, D. K., and Jones, D. B. A.: Effects of a priori profile shape
308 assumptions on comparisons between satellite NO₂ columns and model simulations, *Atmos.*
309 *Chem. Phys.*, 20, 7231–7241, <https://doi.org/10.5194/acp-20-7231-2020>, 2020a.
310
311 Cooper, M. J., Martin, R. V., McLinden, C. A., and Brook, J. R.: Inferring ground-level nitrogen
312 dioxide concentrations at fine spatial resolution applied to the TROPOMI satellite instrument,
313 *Environ. Res. Lett.*, 15, 104013, <https://doi.org/10.1088/1748-9326/aba3a5>, 2020b.
314
315 Dang, R., Jacob, D. J., Shah, V., Eastham, S. D., Fritz, T. M., Mickley, L. J., Liu, T., Wang, Y., and
316 Wang, J.: Background nitrogen dioxide (NO₂) over the United States and its implications for
317 satellite observations and trends: effects of nitrate photolysis, aircraft, and open fires, *Atmos.*
318 *Chem. Phys.*, 23, 6271–6284, <https://doi.org/10.5194/acp-23-6271-2023>, 2023.
319
320 Duncan, B. N., Lamsal, L. N., Thompson, A. M., Yoshida, Y., Lu, Z., Streets, D. G., Hurwitz, M. M.,
321 and Pickering, K. E.: A space-based, high-resolution view of notable changes in urban NO_x
322 pollution around the world (2005–2014), *J. Geophys. Res.-Atmos.*, 121, 976–996,
323 <https://doi.org/10.1002/2015JD024121>, 2016.
324
325 Fiedler, S. E., Hese, A., and Ruth, A. A.: Incoherent broad-band cavity-enhanced absorption
326 spectroscopy, *Chem. Phys. Lett.*, 371, 284–294, [https://doi.org/10.1016/S0009-2614\(03\)00263-](https://doi.org/10.1016/S0009-2614(03)00263-X)
327 *X*, 2003.
328
329 Hannun, R. A., Swanson, A. K., Bailey, S. A., Hanisco, T. F., Bui, T. P., Bourgeois, I., Peischl, J., and
330 Ryerson, T. B.: A cavity-enhanced ultraviolet absorption instrument for high-precision, fast-time-
331 response ozone measurements, *Atmos. Meas. Tech.*, 13, 6877–6887,
332 <https://doi.org/10.5194/amt-13-6877-2020>, 2020.
333
334 Lampel, J., Pöhler, D., Tschritter, J., Frieß, U., and Platt, U.: On the relative absorption strengths
335 of water vapour in the blue wavelength range, *Atmos. Meas. Tech.*, 8, 4329–4346,
336 <https://doi.org/10.5194/amt-8-4329-2015>, 2015.
337
338 Lampel, J., Pöhler, D., Polyansky, O. L., Kyuberis, A. A., Zobov, N. F., Tennyson, J., Lodi, L., Frieß,
339 U., Wang, Y., Beirle, S., Platt, U., and Wagner, T.: Detection of water vapour absorption around
340 363 nm in measured atmospheric absorption spectra and its effect on DOAS evaluations, *Atmos.*
341 *Chem. Phys.*, 17, 1271–1295, <https://doi.org/10.5194/acp-17-1271-2017>, 2017.
342
343 Martin, R. V., Jacob, D. J., Chance, K., Kurosu, T. P., Palmer, P. I., and Evans, M. J.: Global inventory
344 of nitrogen oxide emissions constrained by space-based observations of NO₂ columns, *J.*
345 *Geophys. Res.-Atmos.*, 108, <https://doi.org/10.1029/2003JD003453>, 2003.
346
347 Min, K.-E., Washenfelder, R. A., Dubé, W. P., Langford, A. O., Edwards, P. M., Zarzana, K. J., Stutz,
348 J., Lu, K., Rohrer, F., Zhang, Y., and Brown, S. S.: A broadband cavity enhanced absorption
349 spectrometer for aircraft measurements of glyoxal, methylglyoxal, nitrous acid, nitrogen dioxide,



350 and water vapor, *Atmos. Meas. Tech.*, 9, 423–440, <https://doi.org/10.5194/amt-9-423-2016>,
351 2016.
352
353 Miyazaki, K., Eskes, H., Sudo, K., Boersma, K. F., Bowman, K., and Kanaya, Y.: Decadal changes in
354 global surface NO_x emissions from multi-constituent satellite data assimilation, *Atmos. Chem.*
355 *Phys.*, 17, 807–837, <https://doi.org/10.5194/acp-17-807-2017>, 2017.
356
357 Platt, U. and Kuhn, J.: Caution with spectroscopic NO₂ reference cells (cuvettes), *Atmos. Meas.*
358 *Tech.*, 12, 6259–6272, <https://doi.org/10.5194/amt-12-6259-2019>, 2019.
359
360 Ryerson, T. B., Williams, E. J., and Fehsenfeld, F. C.: An efficient photolysis system for fast-
361 response NO₂ measurements, *J. Geophys. Res.-Atmos.*, 105, 26447–26461,
362 <https://doi.org/10.1029/2000JD900389>, 2000.
363
364 Sluis, W. W., Allaart, M. a. F., Peters, A. J. M., and Gast, L. F. L.: The development of a nitrogen
365 dioxide sonde, *Atmos. Meas. Tech.*, 3, 1753–1762, <https://doi.org/10.5194/amt-3-1753-2010>,
366 2010.
367
368 Spinei, E., Cede, A., Swartz, W. H., Herman, J., and Mount, G. H.: The use of NO₂ absorption cross
369 section temperature sensitivity to derive NO₂ profile temperature and stratospheric–
370 tropospheric column partitioning from visible direct-sun DOAS measurements, *Atmos. Meas.*
371 *Tech.*, 7, 4299–4316, <https://doi.org/10.5194/amt-7-4299-2014>, 2014.
372
373 St. Clair, J. M., Swanson, A. K., Bailey, S. A., and Hanisco, T. F.: CAFE: a new, improved nonresonant
374 laser-induced fluorescence instrument for airborne in situ measurement of formaldehyde,
375 *Atmos. Meas. Tech.*, 12, 4581–4590, <https://doi.org/10.5194/amt-12-4581-2019>, 2019.
376
377 Thornton, J. A., Wooldridge, P. J., and Cohen, R. C.: Atmospheric NO₂: In Situ Laser-Induced
378 Fluorescence Detection at Parts per Trillion Mixing Ratios, *Anal. Chem.*, 72, 528–539,
379 <https://doi.org/10.1021/ac9908905>, 2000.
380
381 Troe, J.: Are Primary Quantum Yields of NO₂ Photolysis at $\lambda \leq 398$ nm Smaller than Unity?, *Z.*
382 *Phys. Chem.*, 214, 573–581, <https://doi.org/10.1524/zpch.2000.214.5.573>, 2000.
383
384 Vandaele, A. C., Hermans, C., Simon, P. C., Carleer, M., Colin, R., Fally, S., Mérianne, M. F.,
385 Jenouvrier, A., and Coquart, B.: Measurements of the NO₂ absorption cross-section from 42 000
386 cm⁻¹ to 10 000 cm⁻¹ (238–1000 nm) at 220 K and 294 K, *J. Quant. Spectrosc. Ra.*, 59, 171–184,
387 [https://doi.org/10.1016/S0022-4073\(97\)00168-4](https://doi.org/10.1016/S0022-4073(97)00168-4), 1998.
388
389 Washenfelder, R. A., Langford, A. O., Fuchs, H., and Brown, S. S.: Measurement of glyoxal using
390 an incoherent broadband cavity enhanced absorption spectrometer, *Atmos. Chem. Phys.*, 8,
391 7779–7793, <https://doi.org/10.5194/acp-8-7779-2008>, 2008.
392



- 393 Wilson, K. L. and Birks, J. W.: Mechanism and Elimination of a Water Vapor Interference in the
394 Measurement of Ozone by UV Absorbance, *Environ. Sci. Technol.*, 40, 6361–6367,
395 <https://doi.org/10.1021/es052590c>, 2006.
396
397 Womack, C. C., Brown, S. S., Ciciora, S. J., Gao, R.-S., McLaughlin, R. J., Robinson, M. A., Rudich,
398 Y., and Washenfelder, R. A.: A lightweight broadband cavity-enhanced spectrometer for NO₂
399 measurement on uncrewed aerial vehicles, *Atmos. Meas. Tech.*, 15, 6643–6652,
400 <https://doi.org/10.5194/amt-15-6643-2022>, 2022.